Article:
Nedelkoski, Zlatko, Sharp, Paul M., do Nascimento, Julio A. et al. (2026) Atomic-scale observation of vacancy ordering in magnetite nanoparticles. Ultramicroscopy. 114332. ISSN: 0304-3991

https://doi.org/10.1016/j.ultramic.2026.114332

Atomic-Scale Observation of Vacancy Ordering in Magnetite Nanoparticles

Zlatko Nedelkoski[a], Paul M. Sharp[b], Julio A. do Nascimento[c], Leonardo Lari[c,g], Philip Hasnip[c], Sara Majetich[d], Quentin M. Ramasse[b,e,f], Demie Kepaptsoglou[b,c,g], Vlado K. Lazarov[c,g*]

[a] Faculty of Technical Sciences, Mother Theresa University, 1669 11A, Skopje, North Macedonia

[b] SuperSTEM, Sci-Tech Daresbury Campus, Daresbury, WA4 4AD, UK

[c] School of Physics Engineering and Technology, University of York, Heslington, YO10 5DD, York, UK

[d] Physics Department, Carnegie Mellon University, Pittsburgh, 15213, Pennsylvania, USA

[e] School of Chemical and Process Engineering, University of Leeds, Leeds LS29JT, UK

[f] School of Physics and Astronomy, University of Leeds, Leeds LS29JT, UK

[g] York-JEOL Nanocentre, University of York, Heslington, YO10 5BR, York, UK

[*]Correspondence: vlado.lazarov@york.ac.uk

Abstract

Magnetic nanoparticles have been extensively investigated for use in various advanced technologies. Among them, magnetite nanoparticles garner significant attention owing to their biocompatibility and superior magnetic properties. However, their performance can be affected by the presence of discrepancies from the ideal bulk structure. In this study, we carried out an atomistic microscopy observation of magnetite nanoparticles by high-angle annular dark field scanning transmission electron microscopy (HAADF-STEM), which demonstrates the formation of vacancies in their structure reflected in changes in the atomic column contrast. In addition, the HAADF-STEM images, acquired along the [111] orientation, demonstrate the tendency of symmetric ordering of the observed vacancies in opposite atomic columns around the central brightest atomic columns. Atomic crystal structure optimization simulations confirm the lowest energies for such ordering configurations, in a good agreement with the experimental observations.

Keywords: magnetite nanoparticles; vacancies; scanning transmission electron microscopy

1. Introduction

Iron oxide nanoparticles (NPs) have desirable properties for numerous applications, including magnetic separation [1], magnetic hyperthermia [2], magnetic resonance imaging [3], use as contrast agents [4, 5], controlled drug delivery [6], and in ferrofluids [7, 8]. Among them, magnetic fluid hyperthermia has attracted particular attention as a very promising method for brain cancer treatment owing to its localized nature compared to conventional methods [9]. For such applications, NPs consisting of magnetite (Fe_3O_4) and maghemite ($\gamma -Fe_2O_3$) structures have been regarded as most suitable owing to their high saturation magnetization, high biocompatibility after surfactant coating, high oxidation resistance, and moderate magnetic anisotropy [10]. Besides these biomedical applications, magnetite has desirable characteristics for use in the form of thin films in spin-electronic devices owing to its high Curie temperature of approximately 858 K, predicted spin polarisation at the Fermi level of 100%, and high abundance of its constituent elements (Fe and O) [11, 12]. However, the properties of these structures in both NP and thin-film forms can significantly change with any alterations from the ideal bulk-like structures [11, 13].

For example, reduced magnetizations, relative to the bulk, have been attributed to surface spin disorder [14, 15] and variations in crystallinity [16]. Spin canting across core/shell $Fe_3O_4/Mn_xFe_{3-x}O_4$ NPs has also been identified as responsible for the observed reduction in magnetization, and its origin has been explained through atomistic simulations [17]. In addition, atomistic models of elongated magnetite nanocrystals with different shapes and surface faceting have elucidated the role of shape anisotropy on the effective magnetic anisotropy energy [18].

Thus, structure control, particularly at the atomic level, is crucial for the provision of the desired performance. However, the synthesis of NPs with a magnetization close to that of bulk magnetite is still a challenging task due to difficulties in the precise control of their stoichiometry and ubiquitous presence of structural defects [13]. For example, strong antiferromagnetic super-exchange interactions across antiphase boundaries significantly decreased the magnetization of magnetite NPs owing to the formation of multiple magnetic domains even in NPs with sizes below 15 nm [13].

In addition, magnetite NPs tend to transform toward the more stable maghemite form of iron oxide. Although both maghemite and magnetite exhibit the same inverse spinel structure, magnetite contains Fe^{2+} and Fe^{3+} cations, while, in maghemite, all iron cations are trivalent and charge neutrality is achieved through cation vacancies. The magnetite unit cell can be expressed by $(Fe^{3+})_8[Fe^{2.5+}]_{16}O_{32}$, where ( ) and [ ] denote tetrahedral and octahedral sites, respectively, while, in the maghemite structure, there are eight octahedral Fe vacancies per three cubic unit cells of magnetite [19].

The ordering of vacancies in maghemite has been investigated by both experimental [20] and theoretical [21] approaches. A theoretical model of vacancy ordering in maghemite has been proposed based on the lithium ferrite $LiFe_5O_8$ structure where the “Li” sites, corresponding to Fe, have an occupancy of 1/3 [21]. In the constructed supercell for maghemite with the *c* axis along the [001] crystallographic direction, equivalent to three unit cells of magnetite stacked along the *c*-axis, there are 12 layers of “Li“ sites each with one “Li” site per supercell. 4 of these 12 sites are

populated with Fe, while 8 are vacancies. Calculations showed that the Fe atoms in these sites are distributed such that, after each populated layer, there are two neighboring layers with vacant "Li" sites. Such a distribution yielded the lowest energy among the considered configurations. This atomic configuration exhibited a reduced magnetic moment per unit cell compared to the magnetite counterpart, in agreement with experimental measurements. However, experimental studies suggest [20] that the distribution of vacancies may be affected by the synthesis method including the temperature and time.

These studies show that the determination of vacancy formation and their potential ordering in the magnetite structure is a challenging task that requires a sophisticated atomic-scale analysis. A technique that can provide the required information on this length scale is scanning transmission electron microscopy (STEM). This state-of-the-art measurement method can achieve sub-Angstrom resolution and thus has been used in various studies for detailed investigations of atomic structures [22–24].

In this study, we investigated small magnetite NPs by STEM. Based on the observations, we developed atomistic models to explain the changes in contrast in the acquired images attributed to the formation of vacancies, and carried out image simulations with the multislice approach to evaluate the validity of the proposed models. We identified the lowest-energy atomic structure through the crystal structure prediction code ChemDASH [25], and compared the obtained results to the high-angle annular dark field (HAADF) STEM images. This approach enables the development of realistic models of the magnetite NP atomic structure, and thus can be used to explain the origin of the reduced performances of these NPs observed in numerous applications and guide further studies for their optimization.

2. Methods

Samples were prepared by the Sun method using the Schlenk line techniques, with inert atmosphere decomposition in high-boiling-point organic solvents, with Fe acetyl acetonate as a precursor and combination of oleic acid and oleyl amine surfactants in benzyl ether, as described in further details elsewhere [26].

HAADF STEM imaging was performed using a Nion UltraSTEM100, operated at 100 kV, with a convergence angle of 30 mrad and probe size of 0.9Å. The HAADF inner and outer collection angles were 76 and 200 mrad, respectively. The obtained atomic-resolution images are sums of stacks of rapidly acquired frames, at a frame rate of 5.1 µs/pix. The images were subsequently aligned for drift and scanning distortions using rigid and nonrigid registration methods [27]. The image in Figure 2 is a sum of 30 such frames. The average atomic column intensities were computed within a circle (as illustrated below) with a fixed radius around each column of interest using the ImageJ software. In total, 14 different central atomic columns were used to demonstrate that opposing satellite atomic columns have most similar intensities. The results are presented as mean $\pm$ standard deviation for each pair of atomic columns.

HAADF-STEM image simulations were performed using the QSTEM multislice code [28] on the calculated cells with and without vacancies, respectively, for a qualitative comparison to the experimental images. The simulated images covered an area of 2 nm × 2 nm and depth of 15 nm. The simulated probe conditions were chosen to match those of the experiment: acceleration voltage of 100 keV, convergence semiangle of 30 mrad, and collection semiangles in the range of 76–200 mrad. Thermal diffuse scattering was included in the simulations with averaging over five frozen phonons.

We performed multistage structure optimizations using the ChemDASH software [25, 29]. We employed the same procedure as in [25], with a three-stage optimization process where only the unit cell is optimized in the first stage (without moving atoms). Both atoms and unit cell are optimized in the second stage. The first two stages use a conjugate gradient algorithm for optimization, whereas the third stage switches to a quasi-Newton algorithm, with the BFGS update method, to optimize the unit cell and atoms. Cell vectors and atomic positions were optimized until the g-norm decreased below 0.075 eV $Å^{-1}$. Once relaxed, new structural arrangements in ChemDASH were accepted or rejected according to the Metropolis criterion: Rand $\leqslant \exp(-\Delta E/kT)$ [25]. For each run of ChemDASH, we considered 1000 structures with $kT = 0.025$ eV.

3. Results

Figure 1 presents HAADF STEM images as well as measured and simulated diffraction patterns of the synthesized Fe_3O_4 NP sample. The overall view in Figure 1a shows that the NPs are uniform in size. The agreement between the simulated and measured diffraction patterns in Figure 1b shows that their structure is inverse spinel, as expected for magnetite. The higher-magnification HAADF STEM image in Figure 1c shows that the NPs are well ordered with a single-crystal structure, without structural domains and extended structural defects such as anti-phase domain boundaries found extensively in both thin film and NP forms of magnetite [13, 30, 31].

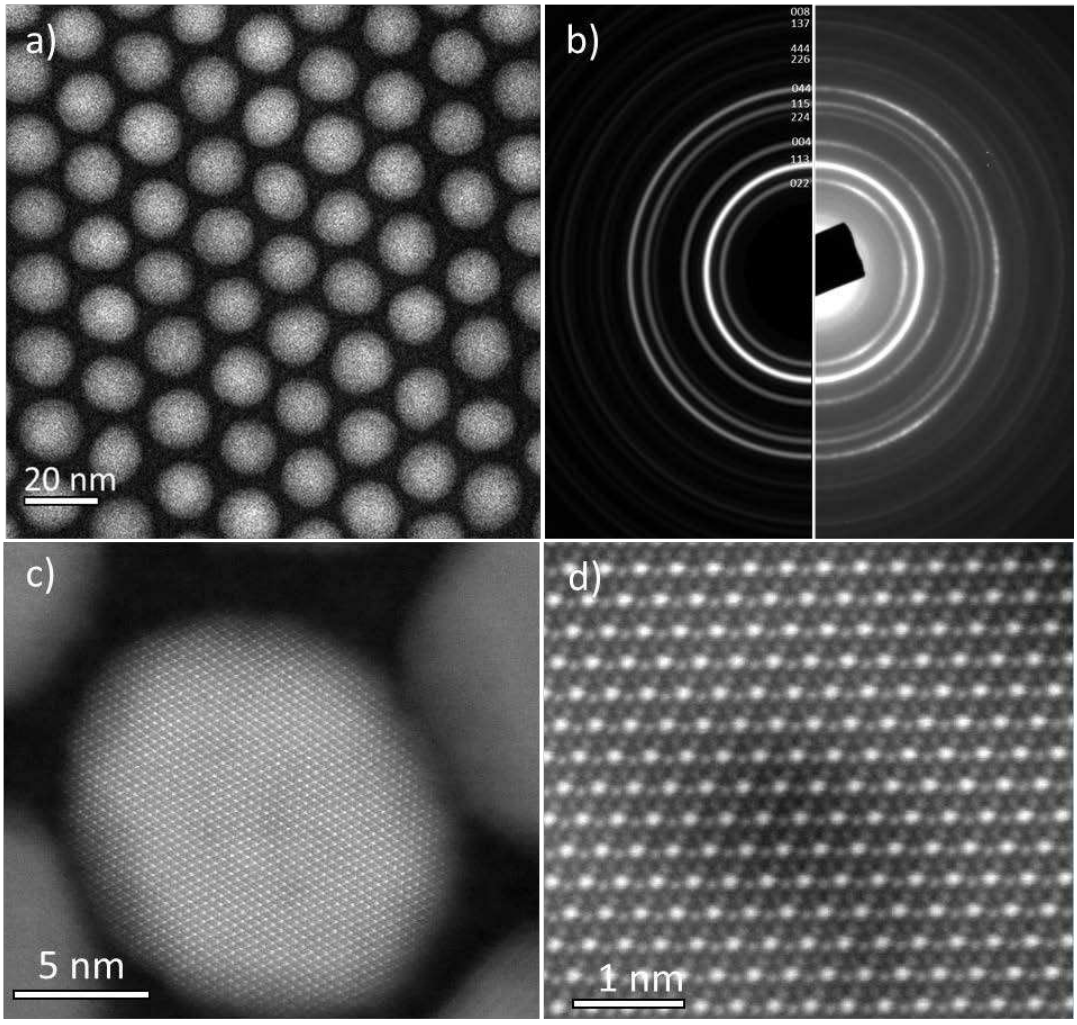

Figure 1. HAADF STEM images and diffraction patterns of the synthesized Fe_3O_4 NPs. a) Overall view, b) (left panel) simulated (magnetite) and (right panel) measured selected-area diffraction patterns (with indexed rings), showing the inverse spinel structure of the Fe_3O_4, c) atomic-resolution HAADF-STEM image of a single Fe_3O_4 particle, and d) high-magnification HAADF STEM image showing the intensity distribution due to the different Fe linear density per atomic column along the [111] direction.

To investigate the atomic structure of the prepared NPs, we carried out an intensity analysis of atomic-resolution HAADF-STEM images. Figure 1d shows an Fe_3O_4 NP oriented along the [111] zone axis. In this orientation, the image shows the expected hexagonal symmetry pattern of the atomic columns of the spinel structure corresponding to different occupations of Fe atoms per unit length. The columns with higher intensities contain three Fe atoms per two O atoms, while those with lower intensities have one Fe atom per two O atoms. For simplicity, the columns with lower intensities are referred to as “satellite” columns, while those with higher intensities are referred to

as “central” columns. However, a more detailed analysis of the images reveals subtle differences in the intensities of the satellite atomic columns, which are expected to be equal.

The investigation of the satellite atomic columns reveals a tendency of symmetric changes in their intensity. To clarify the observed behavior, we denote the six satellite atomic columns as 1–6, as shown in the inset of Figure 2a. In the measured image, we randomly selected 14 central atomic columns and measured the intensities of their satellite atomic columns. For the analysis of each atomic column, we considered the average intensity within a circle centered at that atomic column, as shown in Figure 2a. To understand the changes in the intensity, for each satellite column, we calculated its difference in terms of intensity with respect to the other five atomic columns. For example, the first panel in Figure 2b shows the obtained results for Column 1. This diagram shows that the smallest difference in intensity is obtained with respect to Column 4 (indicated by the red bar). This implies that Column 1 has most similar intensity to Column 4. The other five panels show such analyses for Columns 2–6. Notably, besides the pair 1–4, we also observe similarities for the pairs 2–5 and 3–6. These results demonstrate symmetric changes in intensity around the central atomic columns.

To rule out potential effects of beam exposure on the NP, we divided the image frame dataset containing 30 frames into three subsets, each with 10 frames, shown in Figure S1a–c, which are cumulative images over frames 1–10, 11–20, and 21-30, respectively. The results presented in Supplementary Figure S1 show that opposing satellite columns have most similar intensities in all three stages. This further shows that the observed intensity variation pattern is inherent for the NP, not beam-induced.

Before we address the likely origin of the variation in the satellite atomic column intensities, we note that, in the bulk magnetite structure, the intensity difference between the central and satellite columns is due to the different Fe/O occupations per unit length between those two types of columns, which represent the structure along the [111] direction, as discussed above. Accordingly, in the ideal structure, intensity variations among the satellite atomic columns should not appear.

The significant intensity variations of the satellite columns indicates the presence of Fe vacancies, which can be expected as magnetite NPs tend to transform toward the more stable maghemite structure, with the vacancy content increasing with the progress of the transformation saturating with eight Fe vacancies per three unit cells of magnetite for full transformation to maghemite, gamma-Fe_2O_3. We note that the O sublattice in both maghemite and magnetite has the same characteristic face-centered cubic type of structure. For reference, the bulk atomic structures of magnetite and maghemite are presented and briefly explained in Supplementary Material (Figure S2).

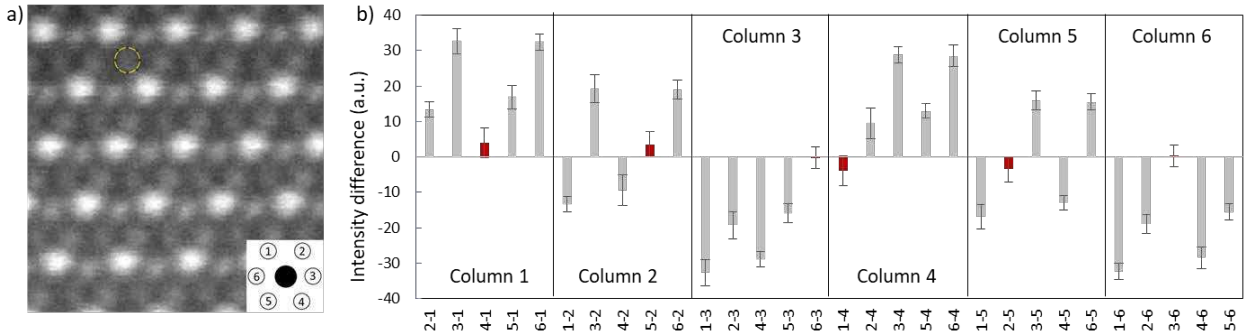

Figure 2. a) Experimental HAADF STEM image of a magnetite NP. The satellite atomic columns around the central column are numbered, from 1 to 6, in the inset for the plots in the right panel. (b) Intensity differences between satellite columns. For example, the plot for Column 1 shows the difference in intensity between Column 1 and other five satellite columns (e.g., 6-1 denotes the difference between the intensity of column 6 and that of column 1, I_6 - I_1). The red bars indicate column pairs with most similar intensities. The yellow circle in (a) was employed to obtain the average intensity for each of the columns. 14 central columns were used in the analysis.

Further, we illustrate the atomic structure of Fe_3O_4 in Figures 3a, b along the [100] and [111] crystallographic directions, respectively. Figure 3c shows a simulated HAADF STEM image along the [111] crystallographic direction, with the expected hexagonal symmetry of atomic columns and contrast variation between the two distinct types of columns. The brighter intensities correspond to the central atomic columns, while the positions with weaker intensities correspond to the satellite atomic columns, as a result of the relative occupancy of Fe atoms in these columns, as discussed above.

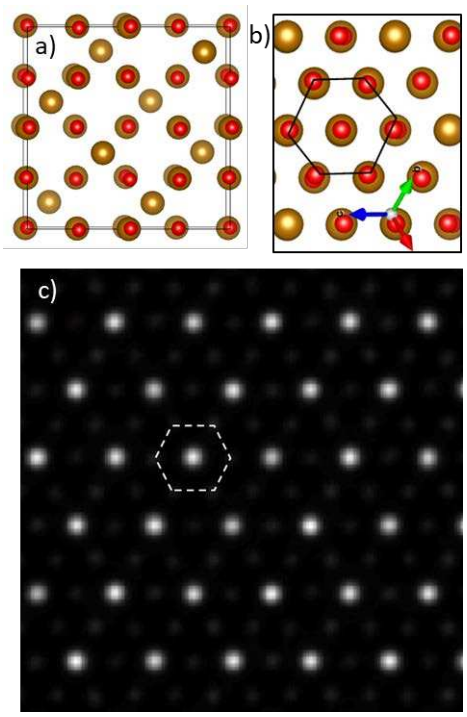

Figure 3. Views of the magnetite structure along the (a) [100] and (b) [111] crystallographic directions. The atoms represented by the large balls are Fe, while those represented by small balls are O atoms. (c) Simulated HAADF STEM image of the fully stoichiometric magnetite structure along the [111] crystallographic direction.

To understand the vacancy formation and their spatial distribution within the "bulk" region of the NPs, we performed a crystal structure prediction analysis. The main goal of these calculations is to identify structural sites of magnetite that are most likely to form thermodynamically stable vacancies. As the maghemite unit cell is basically a three times scaled magnetite along the *c* axis, for a $1 \times 1 \times 3$ supercell of magnetite, we constructed structures containing one or two vacancies. The first vacancy formation can be considered as spatially random within the unit cell, while the second vacancy position is correlated with respect to the first vacancy position to minimize the overall energy of the system. For the two-vacancy case, we used the Site–Occupation Disorder (SOD) package [32] to determine inequivalent configurations of vacancy placements within the magnetite structure. The vast number of combinations of Fe^{2+} and Fe^{3+} ions for each of these configurations renders an exhaustive search impractical. Instead, we use the crystal structure prediction code ChemDASH to randomly swap Fe^{2+} and Fe^{3+} ions amongst the octahedral sites, considering 1000 arrangements of the ions for each vacancy combination. ChemDASH has previously been used to find ground states of structures after doping in atomic species [33, 34]. In this study, we apply the code for vacancy doping. Each of these arrangements of the Fe ions was relaxed to its energetic minimum using atomic force fields in GULP [35]. We employed a force field based on partial charges [36], with parameters presented in Table 1. For the optimization, Buckingham potentials are employed with a cut-off of 10 Å.

Table 1. Buckingham force-field parameters used for the partial charge potential obtained from the literature [36].

Interaction (i–j)	q_i (e)	A_{ij} (eV)	ρ_{ij} (Å)	C_{ij} (eV Å^{-6})
O^{2-} - O^{2-}	-1.2	1844.0	3436	192.58
Fe^{2+}- O^{2-}	1.2	11777.0	0.2071	21.642
Fe^{3+}- O^{2-}	1.8	19952.0	0.1825	4.6583

For the doping of a single vacancy into a structure consisting of three unit cells of Fe_3O_4, we ran ChemDASH ten times while swapping Fe^{2+} and Fe^{3+} ions, and additional ten times where we swapped the position of the vacancy alongside the Fe^{2+} and Fe^{3+} ions (twenty runs in total). For the cases with two vacancies doped into the structure, we found 15 inequivalent configurations of the two vacancies with SOD. We performed one run of ChemDASH for each of these configurations while swapping Fe^{2+} and Fe^{3+} ions, and further run where we allowed the vacancies to swap as well. We performed each of these runs using the partial potential force field.

For ten lowest-energy structures in each of the two-vacancy runs, we used the multislice code QSTEM [28] to simulate a STEM image along the [111] direction of the structure using parameters mirroring the experimental conditions.

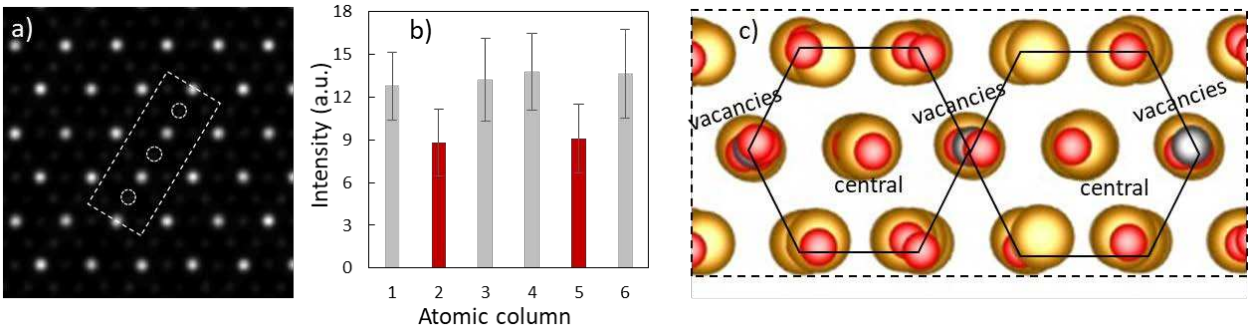

Figure 4. a) Simulated HAADF-STEM image of the optimized NP structure. The vacancy positions are indicated by the white dashed empty circles. b) Average intensities of the six satellite atomic columns. c) Illustration of the optimized atomic model for the region defined by the rectangle in (a). The vacancies are shown in blue, the large balls represent Fe atoms, while the small red balls are oxygen atoms.

Further, we examined the simulated images to evaluate whether the lowest-energy structures found by ChemDASH exhibited the pattern of vacancies observed in the measured STEM images. As shown in Figure 4, the optimization yielded a configuration where the vacancies are symmetrically distributed around the central brightest atomic column, which is further demonstrated by the average intensity analysis of the satellite atomic columns in Figure 4b, showing that the opposite columns 2 and 5 have reduced intensities compared to the other satellite columns. This is consistent with the distribution obtained from the measured STEM image.

Although the calculations are simplified by considering only two vacancies per supercell, the results are in line with the observations. These models represent the initial stage of transformation from magnetite to maghemite. In this study, we consider only compositions close to the magnetite structure as it provides a larger magnetization per unit volume compared to the maghemite structure. The behavior of the distribution at an increased content of vacancies, closer to that of maghemite, could be a subject of further studies.

With the gradual transformation of the magnetite NPs toward maghemite, we expect a gradual reduction in magnetization [20, 21]. Therefore, these subtle differences, in addition to the dominant role of antiphase domain boundaries, could be one of the factors responsible for the lower measured performances of such particles than those expected from ideal magnetite.

The intensity pattern analysis in this study was limited to a single particle. A statistical analysis involving numerous particles is challenging as the initial vacancies can be randomly distributed because the transformation from magnetite toward maghemite is mostly kinetically driven, rather than thermodynamically. This also occurs for the bulk maghemite, exhibiting not only structures with ordered vacancies, but also structures with random vacancy distributions [20, 37]. In addition, the intensity variation pattern along other zone axes may not be as pronounced as that along the [111] zone axis, as demonstrated in Supplementary Figure S3 for the same vacancy distribution along the [1-10] zone axis. Despite these limitations, the acquired data combined with the theoretical modelling provide an evidence on the tendency of the initial stage of vacancy ordering, and pave the way for further more detailed studies involving hundreds of particles and theoretical models with a larger number of vacancies.

4. Conclusion

In this study, we performed electron microscopy observations to evaluate the atomic structure of small magnetite NPs. The intensity analysis of the measured images demonstrates the formation of vacancies in their structure reflected in changes in the atomic column contrast. Notably, the results reveal a tendency of symmetric ordering of the vacancies in satellite atomic columns around the central brightest atomic columns. Atomic crystal structure optimizations show lowest energies for such ordering configurations. The vacancies in the ideal magnetite structure could explain the lower performances in application scenarios than those expected for ideal bulk-like structures. These findings can be valuable in the development of novel methods for structure and property optimization of such NPs, and can guide further studies to broaden their applications.

Acknowledgements

SuperSTEM is the National Research Facility for Advanced Electron Microscopy supported in part by the Engineering and Physical Sciences Research Council (EPSRC) under grant number EP/W021080/1. The Viking cluster was used during this project, which is a high-performance compute facility provided by the University of York. We are grateful for the computational support

from the University of York, IT Services and Research IT team. We also acknowledge the support by EPSRC (Grant No. EP/ S033394/1).

Data Availability

The data are available from the corresponding author upon reasonable request.

Author Contributions

Zlatko Nedelkoski: Data curation, Formal analysis, Writing – original draft, Writing – review and editing; **Paul M. Sharp:** Data curation, Formal analysis, Writing – original draft; **Julio A. do Nascimento**: Formal analysis; **Leonardo Lari**: Formal analysis, Data curation; **Philip Hasnip**: Formal analysis; **Sara Majetich**: Formal analysis, Methodology, Resources; **Quentin M. Ramasse**: Formal analysis, Methodology, Resources, Writing – review and editing; **Demie Kepaptsoglou**: Formal analysis, Methodology, Resources, Data curation, Writing – review and editing; **Vlado K. Lazarov**: Conceptualization, Formal analysis, Resources, Writing – original draft, Writing – review and editing.

References

[1] A.K. Gupta, M. Gupta, Synthesis and surface engineering of iron oxide nanoparticles for biomedical applications, Biomaterials 26 (2005) 3995.

[2] B. Thiesen, A. Jordan, Clinical applications of magnetic nanoparticles for hyperthermia, Int. J. Hypertherm.: Offic. J. Eur. Soc. Hypertherm. Oncol., N. Am. Hypertherm. Gr. 24 (2008) 467.

[3] Q.A. Pankhurst, N.T.K. Thanh, S.K. Jones, J. Dobson, Progress in applications of magnetic nanoparticles in biomedicine, J. Phys. D: Appl. Phys. 42 (2009) 224001.

[4] S. Laurent, D. Forge, M. Port, A. Roch, C. Robic, L. Vander Elst, R.N. Muller, Magnetic iron oxide nanoparticles: synthesis, stabilization, vectorization, physicochemical characterizations, and biological applications, Chem. Rev. 108 (2008) 2064.

[5] C. Pereira, A.M. Pereira, M. Rocha, C. Freire, C.F.G.C. Geraldes, Architectured design of superparamagnetic Fe_3O_4 nanoparticles for application as MRI contrast agents: mastering size and magnetism for enhanced relaxivity, J. Mater. Chem. B 30 (2015).

[6] C.S. Kumar, F. Mohammad, Magnetic nanomaterials for hyperthermia-based therapy and controlled drug delivery, Adv. Drug Deliv. Rev. 63 (2011) 789–808.

[7] P. Berger, N.B. Adelman, K.J. Beckman, D.J. Campbell, A.B. Ellis, G.C. Lisensky, Preparation and properties of an aqueous ferrofluid, J. Chem. Ed. 76 (1999) 943.

[8] K. Raj, B. Moskowitz, R. Casciari, Advances in ferrofluid technology, J. Magn. Magn. Mater. 149 (1995) 174.

[9] S. Dutz, R. Hergt, Magnetic particle hyperthermia — a promising tumour therapy? Nanotechnology 25 (2014) 452001.

[10] S. Laurent, S. Dutz, U.O. Hafeli, M. Mahmoudi, Magnetic fluid hyperthermia: focus on superparamagnetic iron oxide nanoparticles, Adv. Colloid Interface Sci. 166 (2011) 8–23.

[11] D. Gilks, Z. Nedelkoski, L. Lari, B. Kuerbanjiang, K. Matsuzaki, T. Susaki, D. Kepaptsoglou, Q. Ramasse, R. Evans, K. McKenna, V.K. Lazarov, Atomic and electronic structure of twin growth defects in magnetite, Sci. Rep. 6 (2016) 20943.

[12] V.K. Lazarov, M. Weinert, S.A. Chambers, M. Gajdardziska-Josifovska, Atomic and electronic structure of the Fe_3O_4(111)/MgO(111) model polar oxide interface, Phys. Rev. B 72 (2005) 195401.

[13] Z. Nedelkoski, D. Kepaptsoglou, L. Lari, T. Wen, R.A. Booth, S.D. Oberdick, P.L. Galindo, Q.M. Ramasse, R.F.L. Evans, S. Majetich, V.K. Lazarov, Origin of reduced magnetization and domain formation in small magnetite nanoparticles, Sci. Rep. 7 (2017) 45997.

[14] A. Pratt, L. Lari, O. Hovorka, A. Shah, C. Woffinden, S.P. Tear, C. Binns, R. Kröger, Enhanced oxidation of nanoparticles through strain-mediated ionic transport, Nat. Mater. 13 (2014) 26.

[15] R.H. Kodama, A.E. Berkowitz, J.E.J. McNiff, S. Foner, Surface spin disorder in $NiFe_2O_4$ nanoparticles, Phys. Rev. Lett. 77 (1996) 394.

[16] R. Massart, Preparation of aqueous magnetic liquids in alkaline and acidic media, IEEE Trans. Magn. 17 (1981) 1247.

[17] S.D. Oberdick, A. Abdelgawad, C. Moya, S. Mesbahi-Vasey, D. Kepaptsoglou, V.K. Lazarov, R.F.L. Evans, D. Meilak, E. Skoropata, J. van Lierop, I. Hunt-Isaak, H. Pan, Y. Ijiri, K. L. Krycka, J.A. Borchers, S.A. Majetich, Spin canting across core/shell $Fe_3O_4/Mn_xFe_{3-x}O_4$ nanoparticles, Sci. Rep. 8 (2018) 3425.

[18] R. Moreno, S. Poyser, D. Meilak, A. Meo, S. Jenkins, V.K. Lazarov, G. Vallejo-Fernandez, S. Majetich, R.F.L. Evans, The role of faceting and elongation on the magnetic anisotropy of magnetite Fe_3O_4 nanocrystals, Sci. Rep. 10 (2020) 2722.

[19] G.A. Waychunas, Crystal Chemistry of Oxides and Oxyhydroxides, Rev. Mineral. Geochem. 25 (1991) 11.

[20] J.-E. Jørgensen, L. Mosegaard, L.E. Thomsen, T.R. Jensen, J.C. Hanson, Formation of γ-Fe_2O_3 nanoparticles and vacancy ordering: an in situ X-ray powder diffraction study, J. Solid-State Chem. 180 (2007) 180–185.

[21] R. Grau-Crespo, A.Y. Al-Baitai, I. Saadoune, N.H. De Leeuw, Vacancy ordering and electronic structure of γ-Fe_2O_3 (maghemite): a theoretical investigation, J. Phys.: Condens. Matter 22 (2010) 255401.

[22] Z. Nedelkoski, B. Kuerbanjiang, S. E. Glover, A. M. Sanchez, D. Kepaptsoglou, A. Ghasemi, C.W. Burrows, S. Yamada, K. Hamaya, Q.M. Ramasse, P.J. Hasnip, T. Hase, G.R. Bell, A. Hirohata, V.K. Lazarov, Realisation of magnetically and atomically abrupt half-metal/semiconductor interface: $Co_2FeSi_{0.5}Al_{0.5}$/Ge(111), Sci. Rep. 6 (2016) 37282.

[23] D. Gilks, K. P. McKenna, Z. Nedelkoski, B. Kuerbanjiang, K. Matsuzaki, T. Susaki, L. Lari, D. Kepaptsoglou, Q. Ramasse, S. Tear, V.K. Lazarov, Polar spinel–perovskite interfaces: an atomistic study of Fe_3O_4(111)/$SrTiO_3$(111) structure and functionality, Sci. Rep. 6 (2016) 29724.

[24] Z. Nedelkoski, A.M. Sanchez, A. Ghasemi, K. Hamaya, R.F.L. Evans, G.R. Bell, A. Hirohata, V.K. Lazarov, The antiphase boundary in half-metallic Heusler alloy $Co_2Fe(Al,Si)$: atomic structure, spin polarization reversal, and domain wall effects, Appl. Phys. Lett. 109 (2016) 222405.

[25] P.M. Sharp, M.S. Dyer, G.R. Darling, J.B. Claridge, M.J. Rosseinsky, Chemically directed structure evolution for crystal structure prediction, Phys. Chem. Chem. Phys. 22 (2020) 18205–18218.

[26] S. Sun, H. Zeng, D. B. Robinson, S. Raoux, P.M. Rice, S.X. Wang, G. Li, J. Am. Chem. Soc. 126 (2004) 273.

[27] L. Jones, H. Yang, T.J. Pennycook, M.S.J. Marshall, S. Van Aert, N.D. Browning, M.R. Castell, P.D. Nellist, Smart Align — a new tool for robust non-rigid registration of scanning microscope data, Adv. Struct. Chem. Imaging 1 (2015) 8.

[28] C.T. Koch, Determination of core structure periodicity and point defect density along dislocations, Ph.D. thesis, Arizona State University (2002).

[29] J. Gamon, B.B. Duff, M.S. Dyer, C. Collins, L.M. Daniels, T.W. Surta, P.M. Sharp, M.W. Gaultois, F. Blanc, J.B. Claridge, M.J. Rosseinsky, Computationally guided discovery of the sulfide Li_3AlS_3 in the Li–Al–S phase field: structure and lithium conductivity, Chem. Mater. 31 (2019) 9699–9714.

[30] K.P. McKenna, F. Hofer, D. Gilks, V.K. Lazarov, C. Chen, Z. Wang, Y. Ikuhara, Atomic-scale structure and properties of highly stable antiphase boundary defects in Fe_3O_4, Nat. Commun. 5 (2014) 5740.

[31] D. Gilks, L. Lari, J. Naughton, O. Cespedes, Z. Cai, A. Gerber, S.M. Thompson, K. Ziemer, V.K. Lazarov, Origin of anomalous magnetite properties in crystallographic matched heterostructures: Fe_3O_4(111)/$MgAl_2O_4$(111), J. Phys.: Condens. Matter 25 (2013) 485004.

[32] R. Grau-Crespo, S. Hamad, C.R.A. Catlow, N.H. de Leeuw, Symmetry-adapted configurational modelling of fractional site occupancy in solids, J. Phys.: Condens. Matter 19 (2007) 256201.

[33] A. Vasylenko, J. Gamon, B.B. Duff, V.V. Gusev, L.M. Daniels, M. Zanella, J.F. Shin, P.M. Sharp, A. Morscher, R. Chen, A.R. Neale, L.J. Hardwick, J.B. Claridge, F. Blanc, M.W. Gaultois, M.S. Dyer, M.J. Rosseinsky, Element selection for crystalline inorganic solid discovery guided by unsupervised machine learning of experimentally explored chemistry, Nat. Commun. 12 (2021) 5561.

[34] R.C. Dickson, T.D. Manning, E.S. Raj, J.C.S. Booth, M.J. Rosseinsky, M.S. Dyer, Predicting spinel solid solutions using a random atom substitution method, Phys. Chem. Chem. Phys. 24 (2022) 16374– 16387.

[35] J.D. Gale, A.L. Rohl, The general utility lattice program (GULP), Mol. Simulat. 29 (2003) 291–341.

[36] B. Al-Hasni, G. Mountjoy, Structural investigation of iron phosphate glasses using molecular dynamics simulation, J. Noncrystal. Solids 357 (2011) 2775–2779.

[37] I. Kinebuchi, A. Kyono, Study on magnetite oxidation using synchrotron X–ray diffraction and X–ray absorption spectroscopy: vacancy ordering transition in maghemite (γ–Fe_2O_3), J. Miner. Petrolog. Sci. 116(4) (2021) 211–219.